JACS
JOURNAL OF THE AMERICAN CHEMICAL SOCIETY
pubs.acs.org/JACS
Communication

Topochemical Oxidation of Ruddlesden−Popper Nickelates Reveals Distinct Structural Family: Oxygen-Intercalated Layered Perovskites

Dan Ferenc Segedin, Jinkwon Kim, Harrison LaBollita, Nicole K. Taylor, Kyeong-Yoon Baek, Suk Hyun Sung, Ari B. Turkiewicz, Grace A. Pan, Abigail Y. Jiang, Maria Bambrick-Santoyo, Tobias Schwaigert, Casey K. Kim, Anirudh Tenneti, Alexander J. Grutter, Shin Muramoto, Alpha T. N'Diaye, Ismail El Baggari, Donald A. Walko, Charles M. Brooks, Antia S. Botana, Darrell G. Schlom, Hua Zhou, and Julia A. Mundy*

Cite This: J. Am. Chem. Soc. 2026, 148, 5873−5880

ABSTRACT: Layered perovskites—including the Dion−Jacobson, Ruddlesden−Popper, and Aurivillius families—exhibit a wide range of correlated electron phenomena, from high-temperature superconductivity to multiferroicity. Here, we report a new family of layered perovskites realized through topochemical oxidation of $La_{n+1}Ni_nO_{3n+1+\delta}$ (n = 1−4) Ruddlesden−Popper nickelate thin films. Postgrowth ozone annealing induces a substantial c-axis expansion—17.8% for $La_2NiO_{4+\delta}$ (n = 1)—that monotonically decreases with increasing n. Surface synchrotron X-ray diffraction and coherent Bragg rod analysis (COBRA) reveal that this structural expansion arises from the intercalation of approximately $\delta \approx 0.7-1.0$ oxygen atoms into interstitial sites within the rock salt spacer layers, far exceeding the previous record of $\delta \approx 0.3$ for any Ruddlesden−Popper oxide. These oxygen-intercalated phases form a new class of layered perovskites with a spacer layer composition intermediate between the Ruddlesden−Popper and Aurivillius phases. Furthermore, oxygen intercalation induces metallicity, enhances nickel−oxygen hybridization, and suppresses oxygen octahedral rotations, a feature associated with high-temperature superconductivity in Ruddlesden−Popper nickelates. Our work establishes topochemical oxidation as a powerful approach to accessing highly oxidized, metastable phases across a broad range of layered oxide systems, offering new platforms to engineer electronic properties via intercalation chemistry.

INTRODUCTION

Perovskite oxides (ABO_3, A, and B = cation) host an extraordinary range of physical phenomena, from high-temperature superconductivity to room-temperature multiferroicity. These materials also form naturally layered variants, including the Dion−Jacobson,[1,2] Ruddlesden−Popper,[3,4] and Aurivillius[5−8] phases. Among these, the Ruddlesden−Popper family ($A_{n+1}B_nO_{3n+1}$) has been the most extensively studied. These compounds comprise n perovskite ABO_3 layers separated by AO rock salt spacer layers (Figure 1), which tune the effective dimensionality from quasi-2D in A_2BO_4 (n = 1) to 3D in perovskite ABO_3 (n = ∞). Ruddlesden−Popper phases also exhibit emergent properties absent in the perovskite limit, including high-performance tunable dielectrics in titanates,[9] high-temperature superconductivity in cuprates,[10] and more recently, in bilayer and trilayer Ruddlesden−Popper nickelates.[11,12] Beyond dimensionality and epitaxial strain,[13] soft-chemical synthesis methods have demonstrated remarkable tunability in oxides through controlled modification of oxygen content.[14] For example, topochemical reduction of the Ruddlesden−Popper nickelates induces a pronounced structural contraction via oxygen deintercalation, forming the square-planar nickelates—a distinct structural family (Figure S1). These reduced compounds are isoelectronic ($\approx d^9$ filling) and isostructural (square-planar) with the high-T_c, and exhibit superconductivity with notable similarities and differences to the cuprates.[15,16] In contrast, the opposite process—a large structural expansion driven by topochemical oxidation through oxygen intercalation—has not been realized in any Ruddlesden−Popper oxide to date.

RESULTS AND DISCUSSION

Here, we uncover a new family of layered perovskite materials through the topochemical oxidation of Ruddlesden−Popper nickelate thin films. As shown in Figure 1, ozone annealing induces a structural expansion driven by the intercalation of approximately 0.7−1.0 oxygen atoms (δ) per formula unit into interstitial sites within the rock salt spacer layers. This oxygen excess far exceeds the previous record of $\delta \approx 0.3$ for any Ruddlesden−Popper oxide. The resulting structures form a new layered oxide family intermediate between the Ruddlesden−Popper and Aurivillius phases. Additionally, oxygen-intercalated nickelates are metallic with suppressed oxygen octahedral rotations and enhanced nickel−oxygen hybridization, positioning this new family as a promising platform to

Received: July 24, 2025
Revised: January 9, 2026
Accepted: January 12, 2026
Published: February 5, 2026

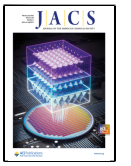

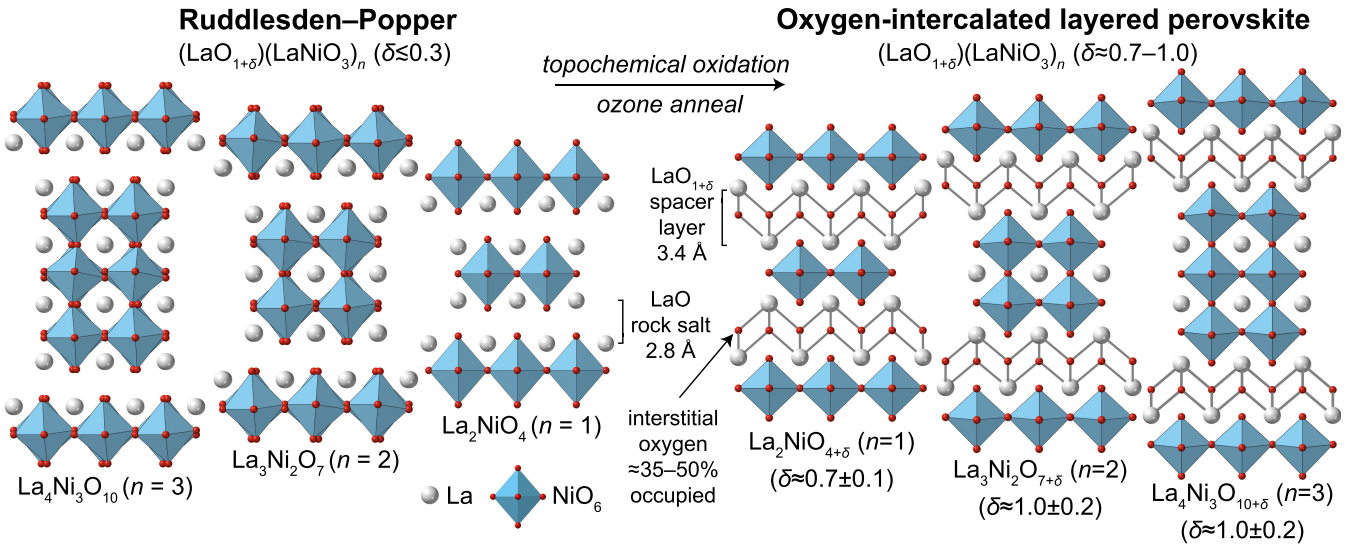

Figure 1. Topochemical oxidation of Ruddlesden–Popper nickelates. Schematic crystal structures of Ruddlesden–Popper (left) and oxygen-intercalated layered perovskite (right) nickelates. Topochemical oxidation induces the intercalation of approximately 0.7–1.0 oxygen atoms per formula unit into interstitial sites within the rock salt layer, driving an expansion of the spacer layer. Approximately 35–50% of the interstitial sites are occupied by oxygen intercalants.

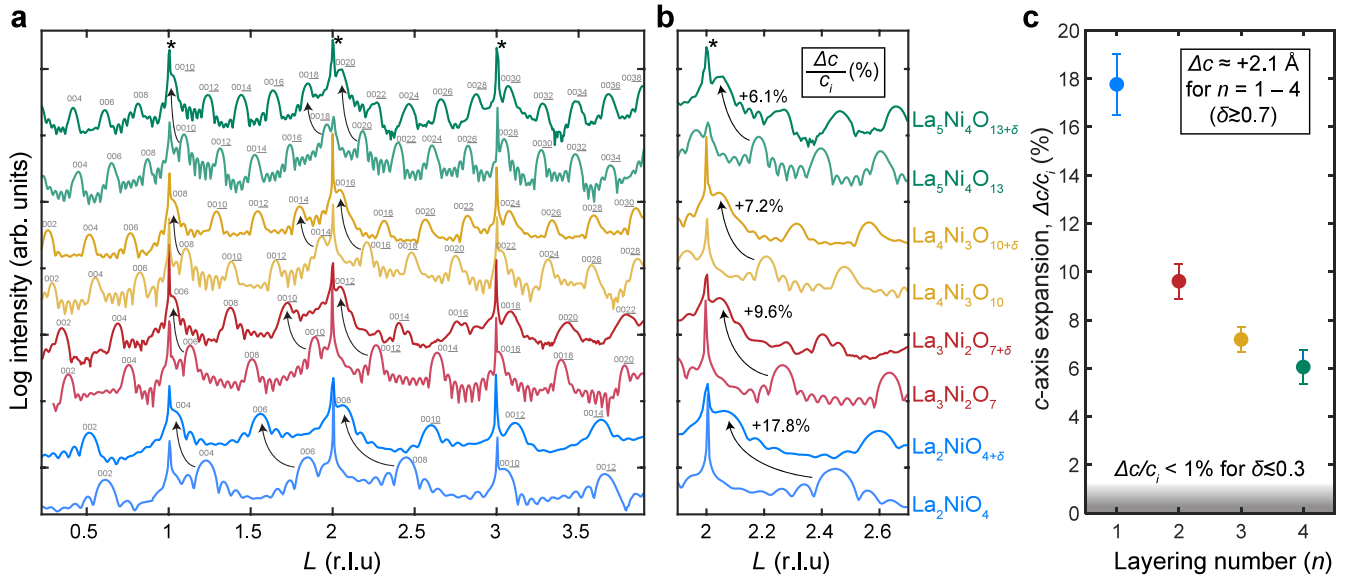

Figure 2. Structural characterization via X-ray diffraction of $La_{n+1}Ni_nO_{3n+1}$ (n = 1–4) films before and after ozone treatment. **a,** Synchrotron X-ray diffraction scans along the (0,0,L) specular crystal truncation rod. **b,** Zoom-in view of scans in **a**. Scans are vertically offset for clarity. Reciprocal space units are normalized to $NdGaO_3$ (110) substrate Bragg peaks, marked with asterisks. Arrows indicate peak shifts following ozone treatment. **c,** Fractional c-axis expansion after oxidation. Lattice constantsand lab-based X-ray scans are available in Table S1 and Figure S2, respectively.

engineer emergent phenomena through intercalation chemistry. Our work also establishes ozone annealing as a powerful synthetic approach to synthesize metastable, highly oxidized phases across a broad family of layered oxides.

We synthesize Ruddlesden–Popper $La_{n+1}Ni_nO_{3n+1}$ (n = 1–4) thin films on $NdGaO_3$ (110) substrates using ozone-assisted molecular-beam epitaxy (MBE). While Ruddlesden–Popper phases with n > 3 are not bulk stable, they can be uniquely stabilized via MBE.[17,18] Subsequent topochemical oxidation is performed via ozone annealing (see methods, Figures S3–S5).

To characterize the structural expansion following ozone annealing, we employed synchrotron surface X-ray diffraction. Figure 2a,b presents (0,0,L) specular crystal truncation rods (CTRs), which probe structural order along the c-axis direction (lab-based X-ray diffraction data are provided in Figure S2). Upon oxidation, all films exhibit pronounced leftward peak shifts, indicative of an increase in the c-axis lattice constant. La_2NiO_4 (n = 1), for example, exhibits a 2.25 Å (17.8%) c-axis expansion from 12.68 to 14.93 Å (see Table S1 for lattice constants). The fractional expansion $\Delta c/c$ decreases monotonically with increasing n, suggesting that expansion occurs primarily within the spacer layers (Figure 2c). The absolute expansion, Δc, is approximately 2.1 ± 0.1 Å for all n values investigated (n = 1–4). In principle, this structural expansion should occur for all n except n = ∞ due to the absence of rock salt layers.

Despite the large c-axis expansion, the $La_{n+1}Ni_nO_{3n+1+\delta}$ films remain epitaxially strained to the substrate following oxidation,

https://doi.org/10.1021/jacs.5c12712
J. Am. Chem. Soc. 2026, 148, 5873–5880

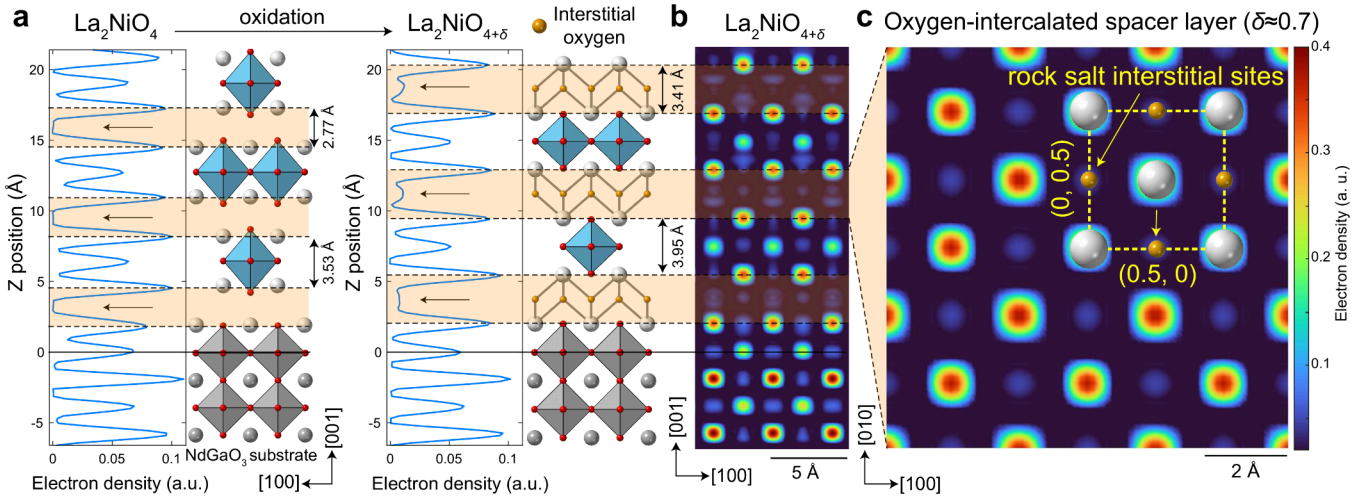

Figure 3. Structural characterization via coherent Bragg rod analysis (COBRA). **a,** Planar-averaged electron density profiles of as-grown (left) and oxidized (right) La_2NiO_4 obtained by 1D-COBRA (Figure S13). Spacer layers are highlighted with gold rectangles. Arrows mark the interstitial positions. Solid lines denote the substrate−film interface. **b,** Projected two-dimensional electron density along the in-plane [010] direction, generated by combining cuts at (a, b) = (0,0) and (0,0.5). **c,** Projected two-dimensional in-plane electron density of the spacer layer, constructed from cuts through the center of the spacer layer and two adjacent LaO planes, as indicated by dashed lines in **b**. The pseudocubic unit cell is represented by the yellow dashed square. 3D-COBRA data in **b** and **c** are generated from nonspecular scans shown in Figure S16.

as indicated by reciprocal space mapping (Figure S6). Furthermore, the reaction proceeds similarly in neodymium-based films (Figure S7) and on other substrates, including $LaAlO_3$ (100) and $SrTiO_3$ (Figure S8), demonstrating the tunability of oxygen-intercalated nickelates via *A*-site substitution and epitaxial strain. Additionally, these phases remain stable with only minor structural degradation after over six months in a nitrogen desiccator (Figure S9) or 18 h in distilled water (Figure S10). Notably, annealing the oxidized films in air restores the parent Ruddlesden−Popper phase, demonstrating the reversibility of the oxidation process (Figure S11).

To determine the structural origin of the *c*-axis expansion, we employ coherent Bragg rod analysis (COBRA) of CTRs.[19,20] We first analyze specular (0,0,*L*) CTRs to determine the planar-averaged electron density profiles for n = 1−3 films. Figure 3a shows the electron density profiles for an n = 1 film, before and after oxidation. In the parent compound, the rock salt spacer layers exhibit no electron density within the rock salt layers. Upon oxidation, the spacer layers expand by 0.64 Å (from 2.77 Å to 3.41 Å, +23.1%) and additionally, electron density emerges between the LaO monolayers, indicating intercalation. The perovskite layers also expand, but by a smaller amount: 0.42 Å (3.53 Å to 3.95 Å, +11.9%). Like the n = 1 film, the oxidized n = 2 and n = 3 films also exhibit expanded spacer layers with an additional electron density (Figure S12). We integrate the interstitial electron density and determine an oxygen excess of 0.7 ± 0.1 for n = 1, 1.0 ± 0.2 for n = 2, and 1.0 ± 0.2 for n = 3 (Figures S12, S13). These results demonstrate that ozone annealing induces an expansion of the spacer layer driven by the intercalation of more than 0.7 oxygen atoms per formula unit. The observed structural expansions are qualitatively reproduced by density functional theory (DFT) calculations of oxygen-intercalated Ruddlesden−Popper nickelates with δ = 1 (Figures S14, S15, Tables S3, S4). Furthermore, we resolve the structure of oxygen-intercalated $La_2NiO_{4+\delta}$ using 3D-COBRA, which reconstructs the three-dimensional electron density from specular and nonspecular CTRs (Figure S16). The projected 2D electron density map in Figure 3b shows localized regions of electron density within the expanded spacer layer corresponding to interstitial oxygen atoms. The in-plane projection of the spacer layer in Figure 3c reveals that the intercalated oxygen atoms occupy rock salt interstitial sites (a, b) = (0, 0.5) and (0.5, 0). The projection along the [110] pseudocubic direction shows additional electron density at (a, b) = (0, 0) (Figure S17). These results demonstrate that intercalated oxygen occupies interstitial sites within the rock salt spacer layers.

Beyond lattice expansion, oxygen intercalation is also expected to modify oxygen octahedral connectivity across the spacer layers. To probe oxygen octahedral rotations, we measure half-order CTRs (h, k = half-integer), which are sensitive to the two-unit-cell periodicity associated with these rotations.[21] We find that following oxidation, half-order peaks vanish for n = 2 and are strongly suppressed for n = 3, indicating that oxygen octahedral rotations are nearly fully quenched for n = 2 and substantially reduced for n = 3 (Figure S18). A similar suppression has been reported in $La_3Ni_{1-x}Co_xO_{7+\delta}$ ($\delta \approx 0.3$), indicating that modest interstitial oxygen content can suppress oxygen octahedral rotations without pronounced structural expansion.[22] Notably, suppressed oxygen octahedral rotations have been linked to high-temperature superconductivity in $La_3Ni_2O_7$ and $La_4Ni_3O_{10}$.[11,12] However, interstitial oxygen can suppress superconductivity by introducing excess hole doping.[23] We also note that ozone annealing is crucial to fully oxidize and stabilize superconductivity in bilayer $(La,Pr)_3Ni_2O_7$ films, though excessive oxidation can destabilize the Ruddlesden−Popper phase, forming "higher-order" phases.[13,22] We propose that these destabilized phases may be related to the oxygen-intercalated compounds reported here. Together, these results highlight the strong coupling among interstitial oxygen content, oxygen octahedral rotations, and spacer layer expansion. Because oxygen octahedral rotations directly couple to emergent phenomena, including electronic bandwidth, magnetism, and orbital polarization, oxygen intercalation provides a powerful route to tune these degrees of freedom.

https://doi.org/10.1021/jacs.5c12712
J. Am. Chem. Soc. 2026, 148, 5873−5880

Comparing the structures of oygen-intercalated layered nickelates with those of other layered perovskites, we find that these compounds form a new structural family that is intermediate between the Ruddlesden−Popper and Aurivillius phases. As shown in Figure 4, these canonical phases are

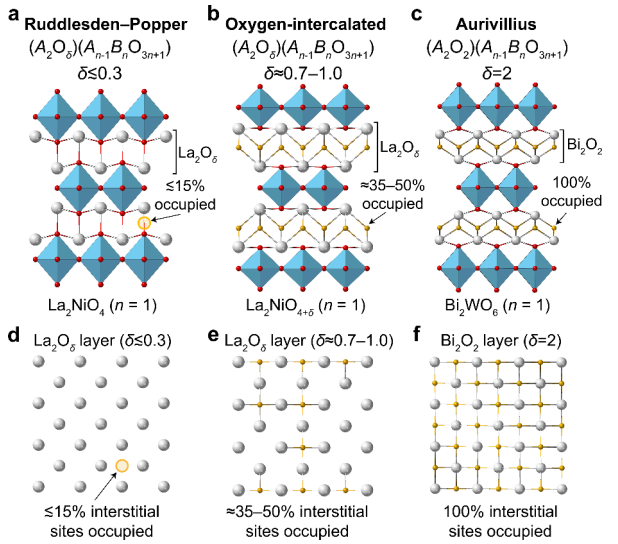

Figure 4. Families of layered perovskites. **a,b,c,** Schematic crystal structures of Ruddlesden−Popper (a), oxygen-intercalated (b), and Aurivillius (c) phases. **d,e,f,** Spacer layer structures for La_2O_δ ($\delta \lesssim 0.3$) (d), La_2O_δ ($\delta \approx 0.3$) (e), and Bi_2O_2 (f). Interstitial sites are marked with gold circles in **a** and **d**. Interstitial and apical oxygen atoms are gold and red, respectively.

distinguished by the composition of the spacer layers that separate the octahedra: A_2O_δ ($\delta \lesssim 0.3$) in Ruddlesden−Popper compounds and A_2O_2 in Aurivillius phases. The A_2O_δ layer forms a square lattice of interstitial sites that are ≲15% occupied in Ruddlesden−Popper (Figure 4d) and fully occupied in Aurivillius compounds (Figure 4f). In contrast, the oxygen-intercalated nickelates adopt an A_2O_δ ($\delta \approx 0.7-1.0$) spacer layer composition (Figure 4b), with ≈ 35−50% interstitial site occupancy (Figure 4e).

To the best of our knowledge, this work provides the first demonstration of a pronounced *c*-axis expansion driven by oxygen intercalation and the largest oxygen excess ($\delta \approx 0.7-1.0$) reported in any Ruddlesden−Popper oxide to date. Prior studies have shown oxygen excess up to $\delta = 0.34$ in $La_2NiO_{4+\delta}$,[24] $\delta = 0.32$ in $La_2CoO_{4+\delta}$,[25] and $\delta = 0.18$ in $La_2CuO_{4+\delta}$,[26] with negligible structural expansion relative to the stoichiometric phase ($\delta = 0$). Whether similarly large oxygen excess and structural expansion can be achieved in bulk powders remains an open question. The thin film platform, in contrast, could be uniquely favorable for topochemical oxidation due to the destabilization of the parent phase via epitaxial strain (Figure S15).

In addition to the intercalation of every spacer layer, as shown in Figure 3, we stabilize a half-oxidized state in $La_2NiO_{4+\delta}$ with stage-2 ordering (intercalation of every two spacer layers). By shortening the ozone-annealing duration, we obtain a $La_2NiO_{4+\delta}$ film with approximately 1 Å (+7.7%) *c*-axis expansion and additional odd-order 00*l* superlattice peaks absent in the fully oxidized film (Figure S19). Similar staging behavior has been reported in $La_2NiO_{4+\delta}$ ($\delta \lesssim 0.3$),[24,26−30] though without pronounced *c*-axis expansion or in-plane oxygen ordering. Detecting additional superlattice peaks or potential in-plane oxygen ordering would require high-dynamical-range reciprocal space mapping (HDRM). In this study, we measure CTRs only at integer or half-integer *h*, *k* values and thus model interstitial oxygen as a homogeneous planar distribution with an average interstitial site occupancy of 35−50% (Figure 3).

Unlike oxygen-rich Ruddlesden−Popper oxides, substantial *c*-axis expansion has been reported in fluorinated[31−33] and

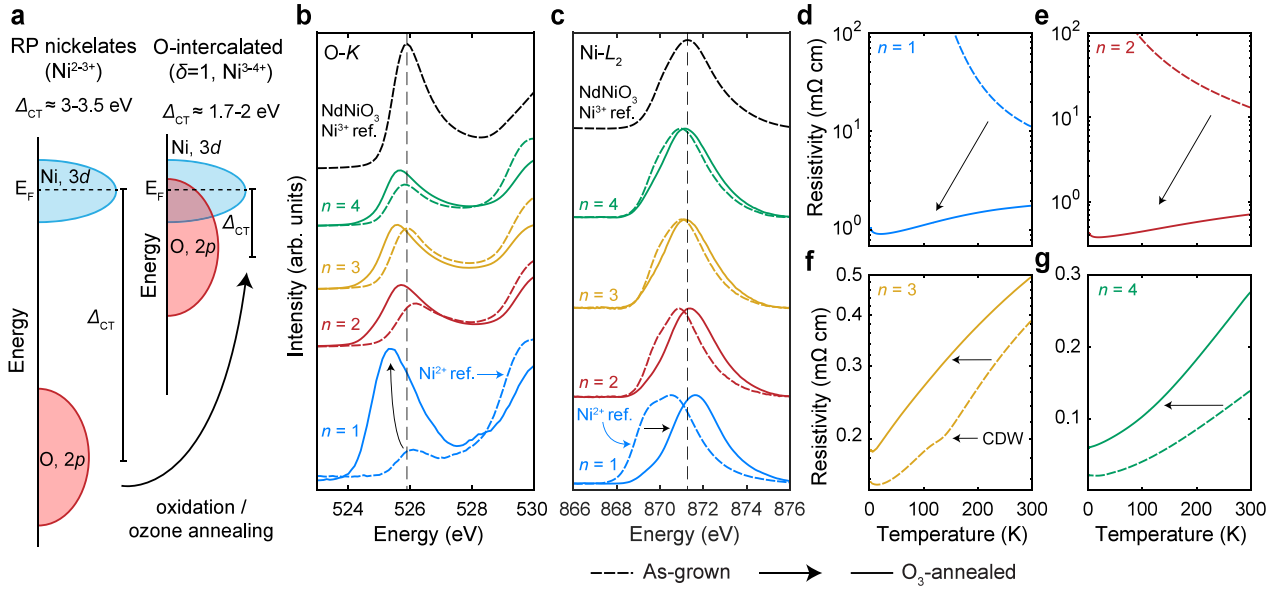

Figure 5. Electronic structure and transport properties of $La_{n+1}Ni_nO_{3n+1+\delta}$ films before and after oxidation. **a,** Schematic electronic structure diagrams of (left) Ruddlesden−Popper and (right) oxygen-intercalated ($\delta = 1$) nickelates calculated via DFT (Supplementary Note 3). X-ray absorption spectra at the **b,** oxygen-*K* edge and **c,** nickel-L_2 edge. The vertical dashed lines in **b** and **c** indicate the nickel 3+ reference peak position. A $NdNiO_3/LaAlO_3$ thin film is used as a nickel 3+ reference. **d,e,f,g,** Temperature-dependent resistivity before and after ozone annealing for $n = 1$ (d), $n = 2$ (e), $n = 3$ (f), and $n = 4$ (g). Dashed and solid lines in **b**−**g** correspond to as-grown and ozone-annealed films, respectively.

https://doi.org/10.1021/jacs.5c12712
J. Am. Chem. Soc. 2026, 148, 5873−5880

hydrated compounds.[34−36] In contrast, fluorinating the single-layer nickelate La_2NiO_4 to $La_2NiO_3F_2$ produces negligible *c*-axis expansion, an effect attributed to strong octahedral distortions that accommodate the intercalated anions.[37] For the oxygen-intercalated nickelates reported here, however, we observe both pronounced *c*-axis expansion and suppressed oxygen octahedral rotations, suggesting a coupling between spacer layer expansion and octahedral rotations (Figure S18).

Next, we examine the electronic structure of oxygen-intercalated nickelates via DFT and X-ray absorption spectroscopy (XAS). As illustrated in Figure 5a, DFT calculations reveal that oxygen intercalation (δ = 1) reduces the charge transfer energy, $\Delta_{CT} = \epsilon_d - \epsilon_p$, from ≈3.0−3.5 eV in the Ruddlesden−Popper nickelates to ≈1.7−2.0 eV in oxygen-intercalated compounds. This reduction reflects an enhancement in nickel−oxygen hybridization (Figure S14). We use the oxygen-*K* edge prepeak to investigate oxidation-induced changes in nickel−oxygen hybridization.[38] Upon oxidation, the prepeak in $La_2NiO_{4+\delta}$ (n = 1) increases in intensity and shifts to lower energy (Figure 5b), indicating an enhancement in nickel−oxygen hybridization and hole doping into hybridized nickel 3*d*−oxygen 2*p* states. This shift decreases with increasing n.

We assess the nickel valence state via spectroscopy at the nickel-L_2 edge.[39] As shown in Figure 5c, the nickel-L_2 edge spectrum shifts toward higher energy after oxidation, surpassing the nickel 3+ reference. Comparison to a nickel 3.4+ reference suggests that the n = 1 sample reaches a similar oxidation state (Figure S20). Like the oxygen-*K* edge, the nickel-L_2 edge shifts diminish with increasing n. These data are consistent with the hypothetical trend $Ni^{+3+0.4/n}$ across the series, assuming La^{3+}, O^{2-}, and oxygen excess $\delta \approx 0.7$ for all RP orders (Figure S21). The larger $\delta \approx 1$ values obtained for n = 2 and n = 3 (Figure S12, Table S2) suggest that the intercalated oxygen may not adopt purely oxide (2−) character but instead peroxide-like (1−) character, consistent with prior reports of peroxide species in oxygen-rich Ruddlesden−Popper oxides.[40−43] Additionally, the XLD signal at the nickel-L_2 edge is suppressed after oxidation (Figure S22), suggesting that oxidation quenches the tetragonal distortion in Ruddlesden−Popper nickelates, as supported by DFT (Figure S14).

Having established the oxidation-induced modifications to the electronic structre, we next investigate the corresponding electrical transport properties. As shown in Figure 5d, the as-grown La_2NiO_4 film is semiconducting, consistent with the antiferromagnetic insulating behavior in bulk form[44] (Supplementary Note 5). Following oxidation, the film becomes metallic. This transition suggests that oxygen intercalation induces hole doping—nominally 1.4 holes per nickel for δ = 0.7—which exceeds the critical doping $x_c \approx 1$ for metallicity in the strontium-doped analogue, $La_{2-x}Sr_xNiO_4$.[45] To the best of our knowledge, this is the first observation of metallicity in an n = 1 Ruddlesden−Popper nickelate in the absence of *A*-site cation substitution. In the n = 2 compound, oxidation similarly drives a semiconductor-to-metal transition (Figure 5e), while in the trilayer, it suppresses the charge-density wave transition (Figures 5f, S23). The four-layer compound maintains its metallicity after oxidation (Figure 5g). We have not observed superconductivity in oxygen-intercalated nickelates to date, likely due to excessive hole doping (Figure S21).

As metallic compounds, oxygen-intercalated nickelates provide a platform for tuning the electronic transport properties through intercalation chemistry. We demonstrate this capability in stage-ordered $La_2NiO_{4+\delta}$, which exhibits increasing electrical conductivity with increasing oxygen content (Figure S19). Oxygen intercalation thus enables controlled modulation of correlated electronic phases with oxygen content, as demonstrated in $La_2CuO_{4+\delta}$ ($\delta \lesssim 0.15$).[46] Whether oxygen insertion in layered nickelates can be pushed beyond $\delta \approx 0.7-1.0$ or precisely tuned remains an open question.

In contrast to oxygen-rich Ruddlesden−Popper nickelates, fluorinated nickelates are insulating to date.[37] We find that fluorination and oxygen intercalation of La_2NiO_4 induce similar *c*-axis expansions but yield insulating and metallic transport, respectively, consistent with prior work (Figure S24).[37] We also note that certain ozone annealing furnaces can result in unintended fluorine incorporation (Figures S24−S26).

Here, we report a new family of oxides—oxygen-intercalated layered perovskites—synthesized through topochemical oxidation of Ruddlesden−Popper nickelates. Oxygen-intercalated nickelates incorporate an unprecedented oxygen excess of approximately 0.7−1.0 atom per formula unit, driving significant *c*-axis expansion and stabilizing a new structural phase intermediate between the Ruddlesden−Popper and Aurivillius families. Oxygen intercalation enhances nickel−oxygen hybridization, suppresses oxygen octahedral rotations, and induces metallicity without chemical substitution, thus establishing a versatile platform for tuning the structure and electronic properties through intercalation chemistry. Moreover, the ability to reversibly oxidize and reduce Ruddlesden−Popper nickelates highlights their exceptional redox activity (Figure S21). Beyond their fundamental significance for oxide electronics, oxygen-intercalated nickelates hold promise for technological applications in solid oxide fuel cells, memristive and ionitronic devices, catalysis, and energy storage, owing to their exceptional reversible redox activity, metallicity, and stability in ambient conditions.[47] Future studies of the ionic conductivity and catalytic activity will further clarify their technological potential. Additionally, oxygen intercalation could provide a path for the exfoliation of layered oxide thin films.[48] More broadly, this work establishes a synthetic route for accessing metastable phases with unusually high oxidation states and novel electronic structures across a wide range of layered oxides.

■ ASSOCIATED CONTENT

Supporting Information

The Supporting Information is available free of charge at https://pubs.acs.org/doi/10.1021/jacs.5c12712.

Methods for thin film synthesis, topochemical oxidation, structural characterization, surface X-ray diffraction, COBRA, electrical transport, and X-ray absorption spectroscopy; additional information on structural characterization, DFT calculations, X-ray absorption spectroscopy, and electrical transport characterization (PDF)

■ AUTHOR INFORMATION

Corresponding Author

Julia A. Mundy − *Department of Physics and School of Engineering and Applied Science, Harvard University, Cambridge, Massachusetts 02138, United States;*

https://doi.org/10.1021/jacs.5c12712
J. Am. Chem. Soc. 2026, 148, 5873−5880

orcid.org/0000-0001-8454-0124; Email: mundy@fas.harvard.edu

Authors

Dan Ferenc Segedin − *Department of Physics, Harvard University, Cambridge, Massachusetts 02138, United States;* orcid.org/0000-0001-7162-8100

Jinkwon Kim − *Department of Materials Science and Engineering, Cornell University, Ithaca, New York 14853, United States*

Harrison LaBollita − *Department of Physics, Arizona State University, Tempe, Arizona 85287, United States; Center for Computational Quantum Physics, Flatiron Institute, New York, New York 10010, United States*

Nicole K. Taylor − *School of Engineering and Applied Science, Harvard University, Cambridge, Massachusetts 02138, United States*

Kyeong-Yoon Baek − *Department of Physics, Harvard University, Cambridge, Massachusetts 02138, United States;* orcid.org/0000-0002-2326-1030

Suk Hyun Sung − *The Rowland Institute at Harvard, Harvard University, Cambridge, Massachusetts 02138, United States*

Ari B. Turkiewicz − *Department of Physics, Harvard University, Cambridge, Massachusetts 02138, United States;* orcid.org/0000-0001-5729-0289

Grace A. Pan − *Department of Physics, Harvard University, Cambridge, Massachusetts 02138, United States;* orcid.org/0000-0002-4512-1215

Abigail Y. Jiang − *School of Engineering and Applied Science, Harvard University, Cambridge, Massachusetts 02138, United States*

Maria Bambrick-Santoyo − *Department of Physics, Harvard University, Cambridge, Massachusetts 02138, United States; Department of Electrical Engineering and Computer Science, Massachusetts Institute of Technology, Cambridge, Massachusetts 02138, United States*

Tobias Schwaigert − *Department of Materials Science and Engineering, Cornell University, Ithaca, New York 14853, United States*

Casey K. Kim − *Department of Materials Science and Engineering, Cornell University, Ithaca, New York 14853, United States*

Anirudh Tenneti − *Smith School of Chemical and Biomolecular Engineering, Cornell University, Ithaca, New York 14853, United States*

Alexander J. Grutter − *NIST Center for Neutron Research, National Institute of Standards and Technology, Gaithersburg, Maryland 20899, United States;* orcid.org/0000-0002-6876-7625

Shin Muramoto − *Material Measurement Laboratory, National Institute of Standards and Technology, Gaithersburg, Maryland 20899, United States;* orcid.org/0000-0003-3135-375X

Alpha T. N'Diaye − *Advanced Light Source, Lawrence Berkeley National Laboratory, Berkeley, California 94720, United States*

Ismail El Baggari − *The Rowland Institute at Harvard, Harvard University, Cambridge, Massachusetts 02138, United States*

Donald A. Walko − *Advanced Photon Source, Argonne National Laboratory, Lemont, Illinois 60439, United States*

Charles M. Brooks − *Department of Physics, Harvard University, Cambridge, Massachusetts 02138, United States*

Antia S. Botana − *Department of Physics, Arizona State University, Tempe, Arizona 85287, United States*

Darrell G. Schlom − *Department of Materials Science and Engineering, Cornell University, Ithaca, New York 14853, United States; Kavli Institute at Cornell for Nanoscale Science, Ithaca, New York 14853, United States; Leibniz-Institut für Kristallzüchtung, 12489 Berlin, Germany;* orcid.org/0000-0003-2493-6113

Hua Zhou − *Advanced Photon Source, Argonne National Laboratory, Lemont, Illinois 60439, United States;* orcid.org/0000-0001-9642-8674

Complete contact information is available at: https://pubs.acs.org/10.1021/jacs.5c12712

Notes

The authors declare no competing financial interest.

■ ACKNOWLEDGMENTS

We thank Michael Hayward for fruitful discussions. This project was primarily supported by the U.S. Department of Energy, Office of Basic Energy Sciences, Division of Materials Sciences and Engineering, under Award No. DE-SC0021925. This work made use of the Advanced Light Source, a U.S. DOE Office of Science User Facility under contract No. DE-AC02-05CH11231. This research was also performed on APS beam time award(s) (DOI: https://doi.org/10.46936/APS-188499/60013161) from the Advanced Photon Source, a U.S. Department of Energy (DOE) Office of Science user facility operated for the DOE Office of Science by Argonne National Laboratory under Contract No. DE-AC02-06CH11357. This work was carried out in part through the use of MIT.nano's facilities and the Harvard University Center for Nanoscale Systems (CNS), a member of the National Nanotechnology Coordinated Infrastructure Network (NNCI), supported by the National Science Foundation under NSF award No. ECCS-2025158. Certain commercial equipment, instruments, software, or materials are identified in this paper in order to specify the experimental procedure adequately. Such identifications are not intended to imply recommendation or endorsement by NIST, nor is it intended to imply that the materials or equipment identified are necessarily the best available for the purpose. D.F.S., G.A.P., and A.Y.J. acknowledge support from the NSF Graduate Research Fellowship No. DGE-1745303. M.B.S. acknowledges support from the NSF Graduate Research Fellowship No. DGE-2141064. N.K.T. and A.Y.J. acknowledge support from the Ford Foundation Predoctoral Fellowship. N.K.T. also acknowledges support from the ALS Doctoral Fellowship in Residence. G.A.P. and A.Y.J. acknowledge support from the Paul and Daisy Soros Fellowship for New Americans. A.B.T. acknowledges support from NSF-DMREF DMR-2323970. S.H.S. and I.E. were supported by the Rowland Institute at Harvard. J.A.M. acknowledges support from the Packard Foundation, Sloan Foundation, and the Gordon and Betty Moore Foundation's EPiQS Initiative, grant GBMF6760. A.S.B. and H.L. acknowledge NSF grant No. DMR-2323971 and the ASU research computing center for HPC resources.

REFERENCES

(1) Dion, M.; Ganne, M.; Tournoux, M. Nouvelles familles de phases $M^{I}M^{II}_{2}$ a Lewandowski "perovskites". *Mater. Res. Bull.* **1981**, *16*, 1429−1435.

(2) Jacobson, A.; Johnson, J. W.; Lewandowski, J. Interlayer chemistry between thick transition-metal oxide layers: synthesis and intercalation reactions of $K[Ca_2Na_{n-3}Nb_nO_{3n+1}]$ ($3 \le n \le 7$). *Inorg. Chem.* **1985**, *24*, 3727.

(3) Balz, D.; Plieth, K. Die Struktur des Kaliumnickelfluorids, K_2NiF_4, Zeitschrift für Elektrochemie. *Berichte der Bunsengesellschaft für physikalische Chemie* **1955**, *59*, 545.

(4) Ruddlesden, S. N.; Popper, P. New compounds of the K_2NiF_4 type. *Acta Crystallogr.* **1957**, *10*, 538.

(5) Aurivillius, B. Mixed Bismuth Oxides with Layer lattices I. The structure type of $CaNb_2Bi_2O_9$. *Ark. Kemi* **1950**, *1*, 463.

(6) Aurivillius, B. *Ark. Kemi* **1950**, *1*, 499.

(7) Aurivillius, B. *Ark. Kemi* **1951**, *2*, 519.

(8) Aurivillius, B. *Ark. Kemi* **1953**, *5*, 39.

(9) Lee, C.-H.; Orloff, N. D.; Birol, T.; Zhu, Y.; Goian, V.; Rocas, E.; Haislmaier, R.; Vlahos, E.; Mundy, J. A.; Kourkoutis, L. F.; Nie, Y.; Biegalski, M. D.; Zhang, J.; Bernhagen, M.; Benedek, N. A.; Kim, Y.; Brock, J. D.; Uecker, R.; Xi, X. X.; Gopalan, V.; Nuzhnyy, D.; Kamba, S.; Muller, D. A.; Takeuchi, I.; Booth, J. C.; Fennie, C. J.; Schlom, D. G. Exploiting dimensionality and defect mitigation to create tunable microwave dielectrics. *Nature* **2013**, *502*, 532−536.

(10) Bednorz, J. G.; Müller, K. A. Possible High-T_c superconductivity in the Ba−La−Cu−O system. *Zeitschrift für Physik B Condensed Matter* **1986**, *64*, 189.

(11) Sun, H.; Huo, M.; Hu, X.; Li, J.; Liu, Z.; Han, Y.; Tang, L.; Mao, Z.; Yang, P.; Wang, B.; Cheng, J.; Yao, D.-X.; Zhang, G.-M.; Wang, M. Signatures of superconductivity near 80 K in a nickelate under high pressure. *Nature* **2023**, *621*, 493.

(12) Zhu, Y.; Peng, D.; Zhang, E.; Pan, B.; Chen, X.; Chen, L.; Ren, H.; Liu, F.; Hao, Y.; Li, N.; Xing, Z.; Lan, F.; Han, J.; Wang, J.; Jia, D.; Wo, H.; Gu, Y.; Gu, Y.; Ji, L.; Wang, W.; Gou, H.; Shen, Y.; Ying, T.; Chen, X.; Yang, W.; Cao, H.; Zheng, C.; Zeng, Q.; Guo, J.-g.; Zhao, J. Superconductivity in pressurized trilayer $La_4Ni_3O_{10-\delta}$ single crystals. *Nature* **2024**, *631*, 531.

(13) Ko, E. K.; Yu, Y.; Liu, Y.; Bhatt, L.; Li, J.; Thampy, V.; Kuo, C.-T.; Wang, B. Y.; Lee, Y.; Lee, K.; Lee, J.-S.; Goodge, B. H.; Muller, D. A.; Hwang, H. Y. Signatures of ambient pressure superconductivity in thin film $La_3Ni_2O_7$. *Nature* **2025**, *638*, 935.

(14) Hayward, M. *Comprehensive Inorganic Chemistry II* (Second ed.), Modern Synthesis, p 417 (2013).

(15) Li, D.; Lee, K.; Wang, B. Y.; Osada, M.; Crossley, S.; Lee, H. R.; Cui, Y.; Hikita, Y.; Hwang, H. Y. Superconductivity in an infinite-layer nickelate. *Nature* **2019**, *572*, 624.

(16) Pan, G. A.; Segedin, D. F.; LaBollita, H.; Song, Q.; Nica, E. M.; Goodge, B. H.; Pierce, A. T.; Doyle, S.; Novakov, S.; Carrizales, D. C.; N'Diaye, A. T.; Shafer, P.; Paik, H.; Heron, J. T.; Mason, J. A.; Yacoby, A.; Kourkoutis, L. F.; Erten, O.; Brooks, C. M.; Botana, A. S.; Mundy, J. A. Superconductivity in a quintuple-layer square-planar nickelate. *Nat. Mater.* **2022**, *21*, 160.

(17) Pan, G. A.; Song, Q.; Segedin, D. F.; Jung, M.-C.; El-Sherif, H.; Fleck, E. E.; Goodge, B. H.; Doyle, S.; Carrizales, D. C.; N'Diaye, A. T.; Shafer, P.; Paik, H.; Kourkoutis, L. F.; Baggari, I. E.; Botana, A. S.; Brooks, C. M.; Mundy, J. A. Synthesis and electronic properties of $Nd_{n+1}Ni_nO_{3n+1}$ Ruddlesden-Popper nickelate thin films. *Physical Review Materials* **2022**, *6*, 055003.

(18) Sun, W.; Li, Y.; Cai, X.; Yang, J.; Guo, W.; Gu, Z.; Zhu, Y.; Nie, Y. Electronic and transport properties in Ruddlesden−Popper neodymium nickelates $Nd_{n+1}Ni_nO_{3n+1}$ (n = 1−5). *Phys. Rev. B* **2021**, *104*, 184518.

(19) Yacoby, Y.; Sowwan, M.; Stern, E.; Cross, J. O.; Brewe, D.; Pindak, R.; Pitney, J.; Dufresne, E. M.; Clarke, R. Direct determination of epitaxial interface structure in Gd_2O_3 passivation of GaAs. *Nat. Mater.* **2002**, *1*, 99.

(20) Zhou, H.; Yacoby, Y.; Butko, V. Y.; Logvenov, G.; Božović, I.; Pindak, R. Anomalous expansion of the copper-apical-oxygen distance in superconducting cuprate bilayers. *Proc. Natl. Acad. Sci. U. S. A.* **2010**, *107*, 8103.

(21) May, S. J.; Kim, J.-W.; Rondinelli, J. M.; Karapetrova, E.; Spaldin, N. A.; Bhattacharya, A.; Ryan, P. J. Quantifying octahedral rotations in strained perovskite oxide films. *Phys. Rev. B* **2010**, *82*, 014110.

(22) Liu, Y.; Ko, E. K.; Tarn, Y.; Bhatt, L.; Li, J.; Thampy, V.; Goodge, B. H.; Muller, D. A.; Raghu, S.; Yu, Y.; Hwang, H. Y. Superconductivity and normal-state transport in compressively strained $La_2PrNi_2O_7$ thin films, *Nat. Mater., 1* (**2025**), 2032

(23) Dong, Z.; Wang, G.; Wang, N.; Dong, W.-H.; Gu, L.; Xu, Y.; Cheng, J.; Chen, Z.; Wang, Y. Interstitial oxygen order and its competition with superconductivity in $La_2PrNi_2O_{7+\delta}$, *Nat. Mater., 1* (**2025**), DOI: 10.1038/s41563-025-02351-2

(24) Aguadero, A.; Alonso, J. A.; Martínez-Lope, M. J.; Fernández-Díaz, M. T.; Escudero, M. J.; Daza, L. In situ high temperature neutron powder diffraction study of oxygen-rich $La_2NiO_{4+\delta}$ in air: correlation with the electrical behaviour. *J. Mater. Chem.* **2006**, *16*, 3402.

(25) Aguadero, A.; Alonso, J. A.; Daza, L. Oxygen Excess in $La_2CoO_{4+\delta}$: A Neutron Diffraction Study. *Zeitschrift für Naturforschung B* **2008**, *63*, 615.

(26) Jorgensen, J. D.; Dabrowski, B.; Pei, S.; Hinks, D. G.; Soderholm, L.; Morosin, B.; Schirber, J. E.; Venturini, E. L.; Ginley, D. S. Superconducting phase of $La_2CuO_{4+\delta}$: A superconducting composition resulting from phase separation. *Phys. Rev. B* **1988**, *38*, 11337.

(27) Hosoya, S.; Omata, T.; Nakajima, K.; Yamada, K.; Endoh, Y. Oxygen doping and phase separation in $La_2NiO_{4+\delta}$. *Physica C: Superconductivity* **1992**, *202*, 188.

(28) Rice, D.; Buttrey, D. An X-Ray Diffraction Study of the Oxygen Content Phase Diagram of $La_2NiO_{4+\delta}$. *J. Solid State Chem.* **1993**, *105*, 197.

(29) Tamura, H.; Hayashi, A.; Ueda, Y. Phase diagram of $La_2NiO_{4+\delta}$ ($0 \le \delta \le 0.18$) I. Phase at room temperature and phases transition above (δ = 0.15). *Physica C: Superconductivity* **1993**, *216*, 83.

(30) Mehta, A.; Heaney, P. J. Structure of $La_2NiO_{4.18}$. *Phys. Rev. B* **1994**, *49*, 563.

(31) Slater, P. R.; Gover, R. K. B. Synthesis and structure of the new oxide fluoride $Sr_2TiO_3F_2$ from the low temperature fluorination of Sr_2TiO_4: an example of a staged fluorine substitution/insertion reaction. *J. Mater. Chem.* **2002**, *12*, 291.

(32) Nowroozi, M. A.; Wissel, K.; Rohrer, J.; Munnangi, A. R.; Clemens, O. $LaSrMnO_4$: Reversible Electrochemical Intercalation of Fluoride Ions in the Context of Fluoride Ion Batteries. *Chem. Mater.* **2017**, *29*, 3441.

(33) Wissel, K.; Vogel, T.; Dasgupta, S.; Fortes, A. D.; Slater, P. R.; Clemens, O. Topochemical Fluorination of n = 2 Ruddlesden−Popper Type $Sr_3Ti_2O_7$ to $Sr_3Ti_2O_5F_4$ and Its Reductive Defluorination. *Inorg. Chem.* **2020**, *59*, 1153.

(34) Slater, P. R.; Gover, R. K. B. Synthesis and structure of the new oxide fluoride $Ba_2ZrO_3F_2 \cdot xH_2O$ ($x \approx 0.5$). *J. Mater. Chem.* **2001**, *11*, 2035.

(35) Pelloquin, D.; Barrier, N.; Flahaut, D.; Caignaert, V.; Maignan, A. Two New Hydrated Oxyhydroxides $Sr_3Co_{1.7}Ti_{0.3}O_5(OH)_2 \cdot xH_2O$ and $Sr_4Co_{1.6}Ti_{1.4}O_8(OH)_2 \cdot xH_2O$ Derived from the RP n = 2 and 3 Members: Structural and Magnetic Behavior versus Temperature. *Chem. Mater.* **2005**, *17*, 773.

(36) Berry, F. J.; Moore, E.; Mortimer, M.; Ren, X.; Heap, R.; Slater, P.; Thomas, M. F. Synthesis and structural investigation of a new oxide fluoride of composition $Ba_2SnO_{2.5}F_3 \cdot xH_2O$ ($x \approx 0.5$). *J. Solid State Chem.* **2008**, *181*, 2185.

(37) Wissel, K.; Heldt, J.; Groszewicz, P. B.; Dasgupta, S.; Breitzke, H.; Donzelli, M.; Waidha, A. I.; Fortes, A. D.; Rohrer, J.; Slater, P. R.; Buntkowsky, G.; Clemens, O. Topochemical Fluorination of $La_2NiO_{4+\delta}$: Unprecedented Ordering of Oxide and Fluoride Ions in $La_2NiO_3F_2$. *Inorg. Chem.* **2018**, *57*, 6549.

https://doi.org/10.1021/jacs.5c12712
J. Am. Chem. Soc. 2026, 148, 5873−5880

(38) Groot, F. M. F. d.; Grioni, M.; Fuggle, J. C.; Ghijsen, J.; Sawatzky, G. A.; Petersen, H. Oxygen 1*s* X-ray-absorption edges of transition-metal oxides. *Phys. Rev. B* **1989**, *40*, 5715.
(39) Fink, J.; Müller-Heinzerling, T.; Scheerer, B.; Speier, W.; Hillebrecht, F. U.; Fuggle, J. C.; Zaanen, J.; Sawatzky, G. A. 2*p* absorption spectra of the 3*d* elements. *Phys. Rev. B* **1985**, *32*, 4899.
(40) Buttrey, D.; Ganguly, P.; Honig, J.; Rao, C.; Schartman, R.; Subbanna, G. Oxygen excess in layered lanthanide nickelates. *J. Solid State Chem.* **1988**, *74*, 233.
(41) Jorgensen, J. D.; Dabrowski, B.; Pei, S.; Richards, D. R.; Hinks, D. G. Structure of the interstitial oxygen defect in $La_2NiO_{4+\delta}$. *Phys. Rev. B* **1989**, *40*, 2187.
(42) Xie, W.; Lee, Y.-L.; Shao-Horn, Y.; Morgan, D. Oxygen Point Defect Chemistry in Ruddlesden−Popper Oxides $(La_{1-x}Sr_x)_2MO_{4\pm\delta}$ (M = Co, Ni, Cu). *J. Phys. Chem. Lett.* **2016**, *7*, 1939.
(43) Xu, S.; Jacobs, R.; Morgan, D. Factors Controlling Oxygen Interstitial Diffusion in the Ruddlesden−Popper Oxide $La_{2-x}Sr_xNiO_{4+\delta}$. *Chem. Mater.* **2018**, *30*, 7166.
(44) Uchida, M.; Ishizaka, K.; Hansmann, P.; Kaneko, Y.; Ishida, Y.; Yang, X.; Kumai, R.; Toschi, A.; Onose, Y.; Arita, R.; Held, K.; Andersen, O. K.; Shin, S.; Tokura, Y. Pseudogap of Metallic Layered Nickelate $R_{2-x}Sr_xNiO_4$ (*R* = Nd, Eu) Crystals Measured Using Angle-Resolved Photoemission Spectroscopy. *Phys. Rev. Lett.* **2011**, *106*, 027001.
(45) Shinomori, S.; Okimoto, Y.; Kawasaki, M.; Tokura, Y. Insulator−Metal Transition in $La_{2-x}Sr_xNiO_4$. *J. Phys. Soc. Jpn.* **2002**, *71*, 705.
(46) Wells, B. O.; Lee, Y. S.; Kastner, M. A.; Christianson, R. J.; Birgeneau, R. J.; Yamada, K.; Endoh, Y.; Shirane, G. Incommensurate Spin Fluctuations in High-Transition Temperature Superconductors. *Science* **1997**, *277*, 1067.
(47) Riaz, A.; Stangl, A.; Burriel, M.; Mermoux, M. In-situ observation of phase transitions in $La_2NiO_{4+\delta}$ bulk and thin film samples via raman spectroscopy. *Acta Mater.* **2025**, *301*, 121570.
(48) Schaak, R. E.; Mallouk, T. E. Prying Apart Ruddlesden−Popper Phases: Exfoliation into Sheets and Nanotubes for Assembly of Perovskite Thin Films. *Chem. Mater.* **2000**, *12*, 3427.

https://doi.org/10.1021/jacs.5c12712
J. Am. Chem. Soc. 2026, 148, 5873−5880